Neutron irradiation and electrical characterisation of the first 8" silicon pad sensor prototypes for the CMS calorimeter endcap upgrade

The CMS HGCAL collaboration

E-mail: thorben.quast@gmail.com

ABSTRACT: As part of its HL-LHC upgrade program, the CMS collaboration is replacing its existing endcap calorimeters with a high-granularity calorimeter (CE). The new calorimeter is a sampling calorimeter with unprecedented transverse and longitudinal readout for both electromagnetic and hadronic compartments. Due to its compactness, intrinsic time resolution, and radiation hardness, silicon has been chosen as active material for the regions exposed to higher radiation levels. The silicon sensors are fabricated as 20 cm (8") wide hexagonal wafers and are segmented into several hundred pads which are read out individually. As part of the sensor qualification strategy, 8" sensor irradiation with neutrons has been conducted at the Rhode Island Nuclear Science Center (RINSC) and followed by their electrical characterisation in 2020-21. The completion of this important milestone in the CE's R&D program is documented in this paper and it provides detailed account of the associated infrastructure and procedures. The results on the electrical properties of the irradiated CE silicon sensors are presented.

https://doi.org/10.1088/1748-0221/18/08/P08024

Contents

1 Introduction

In the current decade, the Large Hadron Collider [1] (LHC) at CERN will be upgraded to the High-Luminosity LHC (HL-LHC) [2]. Its instantaneous luminosity is designed to reach at least five times the LHC's design value. The increase in both the expected number of pile-up interactions and the anticipated damage due to the enhanced radiation levels will pose significant challenges to the LHC experiments.

The CMS [3] collaboration has undertaken an extensive R&D program to upgrade many parts of the detector. One of the planned upgrades consists of the replacement of the existing endcap calorimeters with a high-granularity calorimeter (CE) [4]. The new CE will consist of 47 sampling layers interspersed with absorber plates and will feature close to six million readout channels. For its compactness, fast signal formation, and acceptable radiation hardness, silicon has been chosen as one of the active materials. Approximately $600\,\mathrm{m}^2$ of it will be deployed in the regions where

integrated fluences up to 1×10^{16} 1-MeV neutron-equivalents per square centimeter (n_{eq}/cm^2) at the end of its 10-year operation at the HL-LHC are expected. Prototypes of silicon-based modules have already been built and were tested with particle beams [5–8].

The silicon sensors will be fabricated as multi-pad, DC-coupled, n-on-p ("p-type"), 8" hexagonal wafers with active thicknesses of $120\,\mu m$, $200\,\mu m$ or $300\,\mu m$. To assess their anticipated degradation over the HL-LHC lifetime, irradiation studies are an integral component to the CE's R&D efforts. However, the irradiation and electrical characterisation of full 8" silicon sensors are not trivial due to their large size and the large number of pads. In fact, previous R&D on the CE silicon sensors' bulk degradation in terms of their leakage currents and depletion voltages was, thus far, limited to testing of small, approximately $1\,cm^2$-sized, single-diode test structures [9, 10]. As part of the CE's prototyping phase in the last few years, the CMS collaboration has developed the required infrastructure and procedures for the irradiation and the electrical characterisation of its 8" silicon sensors. The neutron irradiation was performed at the Rhode Island Nuclear Science Center (RINSC) which offers the necessary infrastructure to expose such large objects up to $\sim 10^{16}\,n_{eq}/cm^2$ within a few hours. Afterwards, the ARRAY system [11] was used for the electrical characterisation of all $\mathcal{O}(100)$ pads on the silicon sensors. In order to reduce the fluence-induced leakage current to measurable levels, the tests were conducted at $-40\,^\circ C$.

This paper is structured as follows: section 2 deals with the CE silicon pad sensor prototypes in terms of their design and the production parameters. Section 3 describes the neutron irradiation of the 8" wafers at RINSC. The electrical test setup based on the ARRAY system and the measurement procedure are documented in section 4. Results on the electrical sensor characteristics and their limitations are discussed in section 5. Finally, the conclusions are given in section 6.

2 Silicon pad sensor prototypes for the CMS endcap calorimeter upgrade

The CMS high granularity calorimeter will be made of more than $600\,m^2$ of planar DC-coupled silicon pad sensors. Starting from 8" circular wafers, the sensors are diced into hexagons. P-type doping of their bulk was chosen due to empirical evidence of superior noise performance after irradiation with respect to n-type doping [12].

The oxygen content of those 8" wafers is reduced with respect to the case of the 6" wafers used for the CMS and ATLAS trackers which, in principle, could impair the sensor's radiation hardness.

In this work, the first version prototypes of hexagonal wafer sensors with the so-called low-density (LD) and high-density (HD) designs were irradiated with neutrons and electrically characterised. Their design is illustrated in figure 1. Each CE silicon sensor is segmented into several hundred pads that constitute the sensitive units. The majority of those pads are shaped as regular hexagons which are drawn as cyan-colored pads in figure 1. Special non-hexagonal structures fill out the sensor periphery. The arrangement of pads on a sensor is enclosed by a set of three guard rings (grounded, floating, biased) which protect the sensor from currents drawn from its dicing edges. The LD sensors were produced from physically thinned p-type float zone silicon wafers. They are segmented into 198 pads, where full hexagonal pads are about $1.2\,cm^2$, and $200\,\mu m$ or $300\,\mu m$ in active thickness. LD sensors will be installed in regions of intermediate radiation levels inside the CE. By contrast, regions with the highest radiation levels will be populated with HD
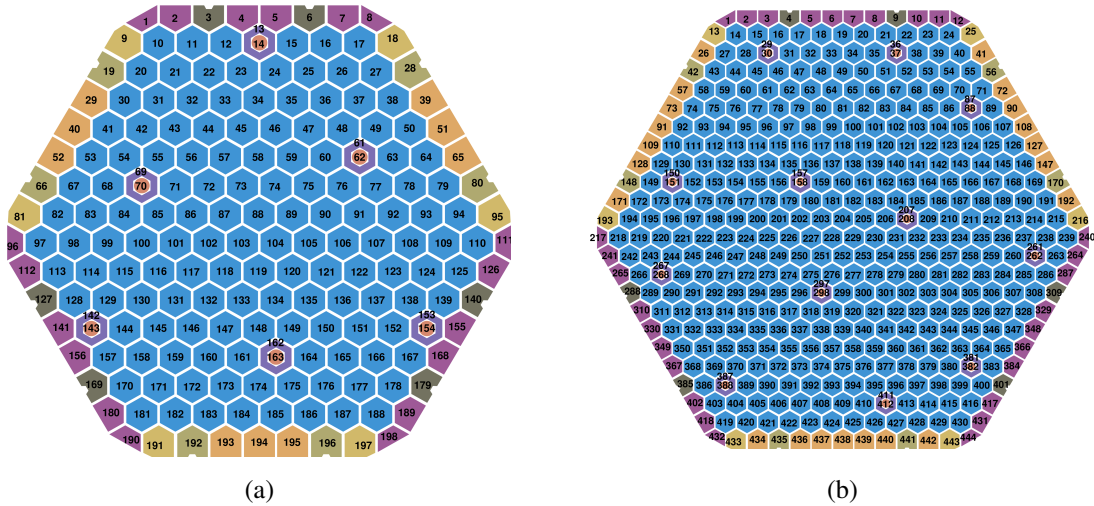
Figure 1. Layout of the tested 8" prototype silicon pad sensors with (a) the low-density (LD) and (b) the high-density (HD) design. Regular-sized hexagonal pads are depicted in cyan. Edge and corner pads populate the sensor periphery. Six (LD), respectively twelve (HD), regular, small hexagonal pads on the sensor are dedicated for energy calibration with minimum ionising particles up to the end of life. The colour coding highlights the different pad geometries. The sensor guard rings are not shown.

sensors whose active thickness is $120\,\mu m$. HD sensors are segmented into 444 pads (full hexagon pad size: $0.5\,cm^2$) and are produced by epitaxial growth.

As it is foreseen for the final design, p-stop structures were added to all the tested prototype silicon sensors in this work in order to limit the accumulation of electrons on the Si/SiO$_2$ interface after exposure to high radiation levels which otherwise could form a conduction channel, effectively shorting adjacent pads. Those structures were either bound to the single pads (individual p-stop) or shared between neighboring ones (common p-stop), representing two options under consideration for the CE. In addition, the tested prototype sensors differed in their flatband voltage (pre-irradiation value of either $-2\,V$ or $-5\,V$). Unless explicitly stated otherwise, all other production parameters, such as doping concentrations and the production process for the oxide material, were identical for all prototype sensors discussed in this paper.

Prior to irradiation, the sensors had been electrically qualified and proper functionality could be verified. In particular, full depletion was achieved around 40 V for $120\,\mu m$ sensors, 120 V for $200\,\mu m$ sensors, and 280 V for $300\,\mu m$ sensors. Moreover, per-pad leakage currents of the non-irradiated sensors did not exceed a few nA, and the total currents at room temperatures between 20–$24\,^\circ C$ over the full sensor remained well below $100\,\mu A$ for (absolute) bias voltages up to 850 V.

In general, exposure of silicon sensors to radiation causes displacement damage to the silicon lattice which affects both the leakage currents and the depletion voltages. While the bulk-dominated leakage current density increases proportionally with the fluence, the expected increase of the depletion voltage (for p-type sensors) is non-trivial and its quantification, like it is done e.g. in refs. [13, 14], is beyond the scope of this work.
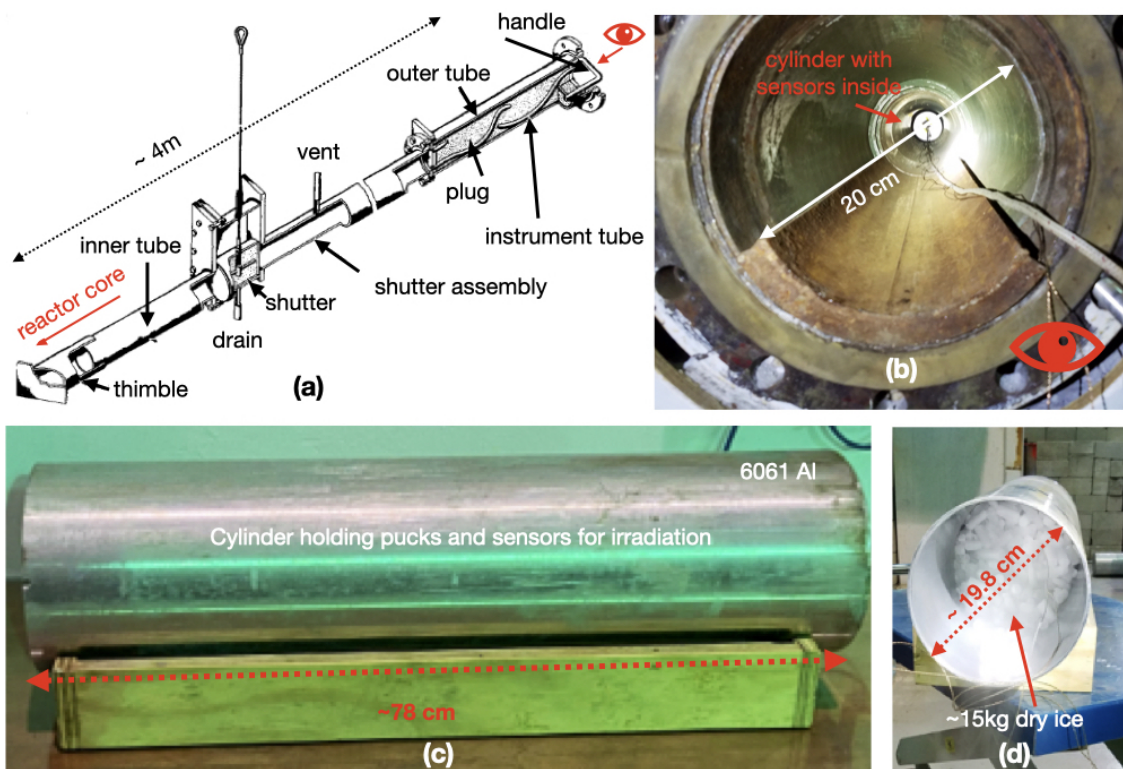
Figure 2. (a) Schematic of the beam port sample delivery system at RINSC. (b) The view into the beam port used for these irradiation studies. (c) The sample delivery cylinder that contains the sensor-holding hockey pucks and (d) dry ice for cooling of the silicon sensors in the beam port during and after irradiation.

3 Irradiation at the Rhode Island Nuclear Science Center

3.1 Rhode Island Nuclear Reactor

The Rhode Island Nuclear Science Center (RINSC) houses a 2 MW, light-water cooled, pool-type reactor in Narragansett, Rhode Island, USA. Its core consists of fuel assemblies moderated with a combination of graphite and beryllium. The fuel is plate type U_3Si_2, cladded with aluminum, enriched to less than 20 % Uranium-235.

The reactor beam port was used as a sample delivery system because it was the only reactor access point large enough to fit a full-sized CE sensor. The beam port in question had not previously been used for experiments, only for facility-related work. A sketch of the beam port and a photo of its inside are shown in figure 2. It measures about 4 m from its opening to the termination near to the reactor core, and it can accommodate samples with diameters of up to 20 cm and with depths up to 90 cm. A shutter assembly is located 3 m from the opening of the beam port, which must be raised to allow for the insertion of the samples and closed prior to the start of operations. A 85 cm-long lead plug serves as a radiation shield that has to be inserted into the opening of the beam port prior to the start of the irradiation.
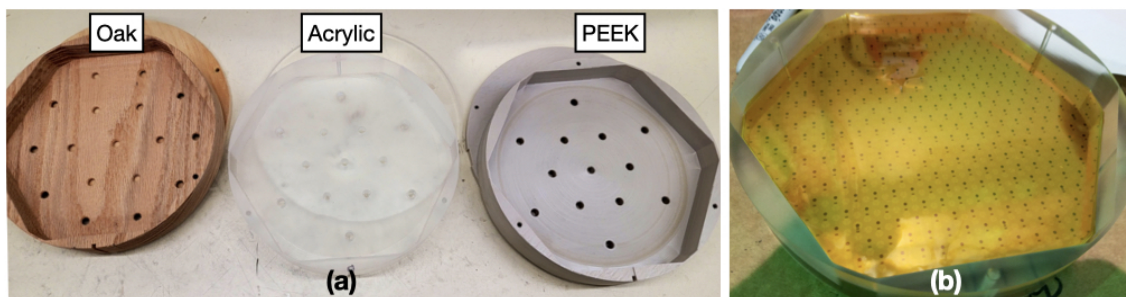
Figure 3. (a) Sample containers ('hockey puck') designed to hold CE silicon sensors for neutron irradiation at RINSC. Wood (oak), acrylic, and PEEK were the puck materials that were experimented with. (b) An 8" high-density CE prototype silicon sensor inside an acrylic puck covered with a Kapton™ foil.

3.2 Irradiation of CE silicon sensor prototypes

Given the constraints of the beam port system at RINSC, a dedicated sample delivery method had to be developed for irradiating CE silicon sensors. This new sample delivery allows for:

- positioning sensors as close to the reactor core as possible;

- protecting them from physical damage during the loading, irradiation, and unloading;

- keeping the irradiated sensors at low temperatures during and after the irradiation;

- monitoring the temperature of the samples inside the beam port.

Two compatible pieces of hardware were manufactured: a sensor container, referred to as a "hockey puck", and a sample delivery cylinder (see figure 2). The former is used to protect, orient, and store the sensors during the irradiation while the latter is used to protect and locate the hockey puck inside the beam port. The cylinder is made from 6061 aluminum and has an outer(inner) diameter of $19.8\,\mathrm{cm}(19.1\,\mathrm{cm})$, allowing for a snug fit of the cylinder inside the beam port and a smooth insertion and removal of the hockey pucks. Three different hockey puck materials were considered (see figure 3): oak, acrylic, and PEEK. They differ in their mechanical properties with respect to temperature and humidity fluctuations, in their activation, radiation hardness and overall cost. As a practical compromise between these factors, acrylic was found most suitable for irradiation up to fluences of $5 \times 10^{15}\,\mathrm{n_{eq}/cm^2}$, and PEEK material suitable for higher fluences. The usage of oak was eventually discarded because of its unfavorable tendency to absorb moisture. The puck base has an outer diameter of 18.6 cm that allows for a smooth fit inside the cylinder. The interior of the puck is milled out in the profile of the silicon sensors with an additional clearance of 1 mm. With these constraints the thinnest sections of the wall of the puck are slightly over 1 mm thick.

Kapton™ foils were used to separate sensors in a stack such that no sensors were in direct contact with any metallic surfaces (cf. figure 3). In addition, antistatic foam was used for covering the top and bottom of the sensor-Kapton™ stack serving as a cushion against the walls inside the puck. After preparation of the puck, the latter was inserted into the delivery cylinder.

In general, the silicon sensors should be kept at low temperatures during the irradiation in order to limit unwanted thermal annealing. For this purpose, the rest of the delivery cylinder
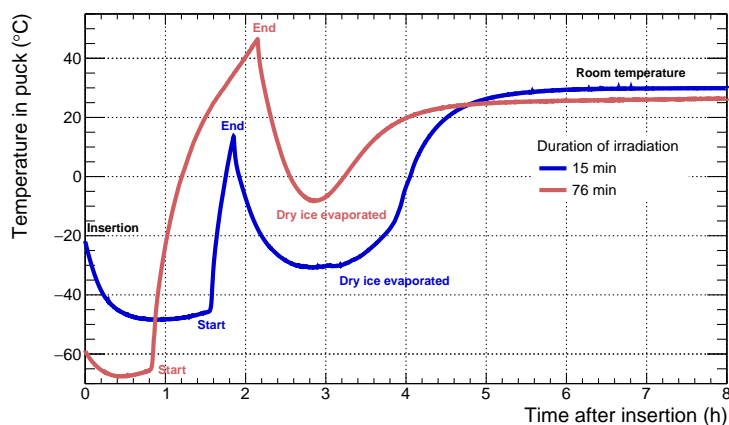
Figure 4. Representative temperature recordings during two of the RINSC irradiation rounds of CE prototype silicon sensors. The time when the irradiation was started and when it ended is indicated. The increase of the temperature towards its plateau coincides with the sublimation of the dry ice inside the delivery cylinder.

was filled with 15-18 kg of dry ice (2). In order to monitor the temperature, PT1000 resistance temperature detectors (RTD) were inserted into the puck, at the front and back faces, to record the temperature throughout the irradiation for assessment of the expected sensor annealing during irradiation. Representative temperature recordings from two irradiation rounds of different duration are shown in figure 4. During irradiation, the temperature rose significantly, eventually reaching temperatures ranging from a few $10\,°C$ to $100\,°C$. In fact, it was found that most of the dry ice sublimated. Only after shutdown of the reactor, the temperature decreased again. As a result, the annealing of the silicon sensors inside the beam port was not negligible. The corresponding annealing time at $60\,°C$, cf. ref. [13], varied between a few minutes to a few hundred minutes for all sensors irradiated at RINSC in 2020-21 up to $\sim 10^{16}$ n_{eq}/cm^2. After 24 h in the beam port after irradiation, the cylinder's activation levels had decayed sufficiently, it could be safely extracted, and transferred into a storage freezer.

3.3 Fluence assessment

In addition to the sensors, mechanical packing material, and temperature sensors, each puck contained a number of reference samples for measuring the fluence achieved during an irradiation round. Two different objects were found appropriate for measuring the fluences during this campaign: silicon diodes, which were studied for usage in the D0 experiment [15], and ultrapure iron foils. The diodes were included inside the puck as close to the sensors as possible by encasing them in small plastic bags and taping them to the inside faces of the puck. By contrast, the iron foils were attached to the exterior of the cylinder for ease of removal and gamma spectroscopy measurements. The latter were performed at RINSC after irradiation for derivation of the integrated fluence. In addition, CV and IV measurements of the irradiated diodes were performed at Brown University to assess the depletion voltage, the associated dark current and ultimately the fluence assuming the literature value for the current-related leakage current rate of $(3.99 \pm 0.03) \times 10^{-17}$ A/cm at $20\,°C$ [13]. The reference silicon diodes are most useful for the lower to medium range of the
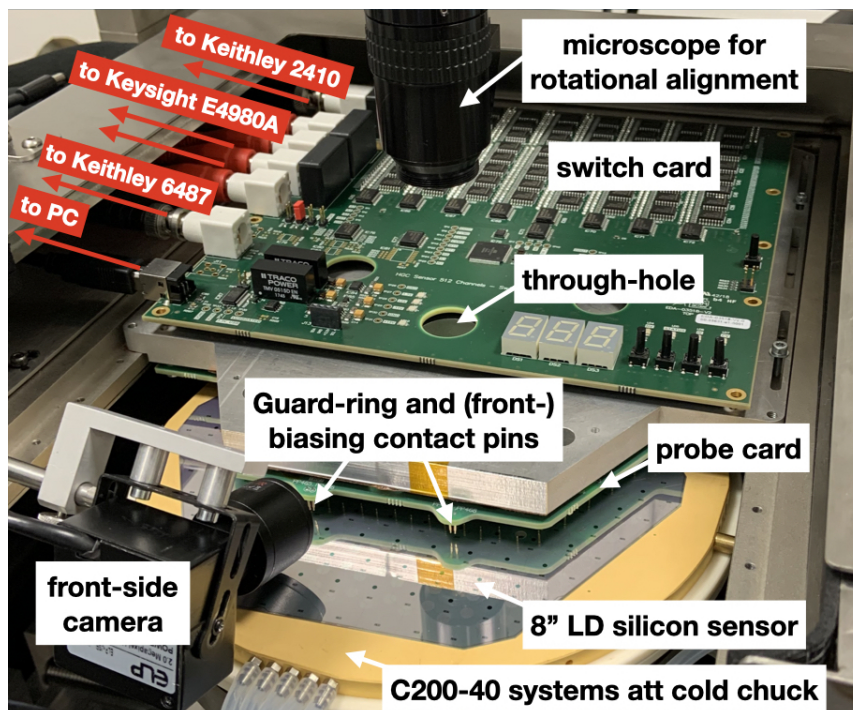
Figure 5. A low-density CE silicon pad sensor right before connecting to the switch- and probe-card based ARRAY system at CERN. The probe station was closed and continuously flushed with dry air during the testing to prevent the formation of ice during low-temperature operation.

targeted fluences, where their depletion voltage was well within the measurement range (< 1000 V). For higher fluences, full depletion of the silicon diodes could not be reached, and the gamma ray spectra derived from the iron foils are considered more reliable. Table 1 in appendix A shows the estimated actual fluences from those reference samples. In order to improve the accuracy of the fluence assessment, future irradiations will include iron foils inside the puck as well as additional silicon test structures.

4   Electrical characterisation of neutron-irradiated silicon pad sensors

The experimental setup and the electrical characterisation procedure of neutron-irradiated CE silicon pad sensors are presented in this section. The following paragraphs describe two similar setups installed at CERN and Texas Tech University, which were used to obtain the results reported in this paper. Since the majority of the results are based on the CERN setup, its specifics are elaborated in the following.

4.1   ARRAY- and cold-chuck based setup at CERN

At CERN, the S200FA probe station produced by Wentworth Laboratories Ltd. was used for the electrical characterisation of neutron-irradiated silicon pad sensors. Its chuck (Systems att, C200-40 model) is temperature-controlled down to $-40\,°\mathrm{C}$. Apart from a Keithley 2410 power supply, a Keithley 6487 picoammeter, and a Keysight E4980A LCR-meter, all relevant components were installed inside the probe station, see figure 5.

The silicon sensors were first placed on the chuck and then connected to the probe- and switch-card based ARRAY system that is described in detail in ref. [11]. The contact between the probe card and the pads was realised with spring-loaded pins. Through-holes in the cards and the probe station's microscope enabled sufficient sensor-to-probe card alignment. Also, the sensor's grounded guard ring was accessible via a dedicated contact pad and could be connected with dedicated pins on the probe card. The high voltage from the power supply was provided to the chuck and with it to the sensor's backside. Two probe cards specific for the LD and HD sensor layouts have been designed and manufactured. The switch card was operated with a bias resistance (R_{bias}) of 1 MΩ and a high voltage resistance (R_{HV}) of 12 kΩ, see ref. [11] (figure 9). In this configuration, the ARRAY system is designed to safely withstand total leakage currents up to 2 mA and per-pad currents up to 10 µA.

Since these limits would have been exceeded by a few orders of magnitude at room temperature, cooling the neutron-irradiated sensors down to −40 °C hereby reducing the leakage current by almost three orders of magnitude with respect to room temperature was imperative. The spatial variation of the C200-40 chuck temperature profile at this temperature amounts to ±0.5 °C, cf. appendix B, whereas fluctuations with time were found to be negligible. For the purpose of preventing the formation of ice, the probe station was continuously flushed with dry air.

With total currents at the order of $O(1\,\text{mA})$, the voltage drop at R_{HV} for the testing of neutron-irradiated sensors corresponded to a few volts and was corrected for. Per-pad leakage currents were measured with the picoammeter, whereas total currents were measured directly with the power supply. The LCR meter was operated at a frequency (f_{LCR}) of 2 kHz for the inference of the per-pad impedance. This particular frequency was chosen to minimise the error associated to the capacitance that is derived from it [11].

4.2 Characterisation procedure

After connecting the sensor to the probecard, per-pad leakage currents as a function of the bias voltage for all pads on a given sensor were measured (IV). This was followed by a per-pad capacitance vs. bias voltage assessment (CV). After each iteration over all pads at a fixed bias voltage, voltages were incremented in varying steps between 50-100 V up to 850 V, whereby the exact choice depended on the measurement type (IV/CV) and on the thickness of the sensor. Although not applicable for the results shown in this work, it should be noted that a given measurement sequence was aborted if the total leakage current exceeded 2 mA. Similarly, individual pads whose leakage currents exceeded 5 µA were not measured any further and in particular were excluded from the subsequent CV. These compliance limits prohibited large voltage drops inside the test circuitry, minimising the risk of damage to the ARRAY system.

The entire characterisation sequence was fully automatised as a LabVIEW-based program (HexDAQ version 1.5.1 [16]). Including voltage ramps and settling times, the IV(CV) measurements of low-density sensors in this work took about 1.5 h(2.5 h), whereby the duration is proportional to the number of voltage steps (10-15 here). The duration was about twice as long for high-density sensors due to the higher number of pads. In order to quantify the potential performance benefit via annealing, silicon sensors were warmed up to 60 °C inside the probe station. After a total of 80 min at this temperature [1], the sensor's depletion voltage is expected to be minimal [17] and the

---

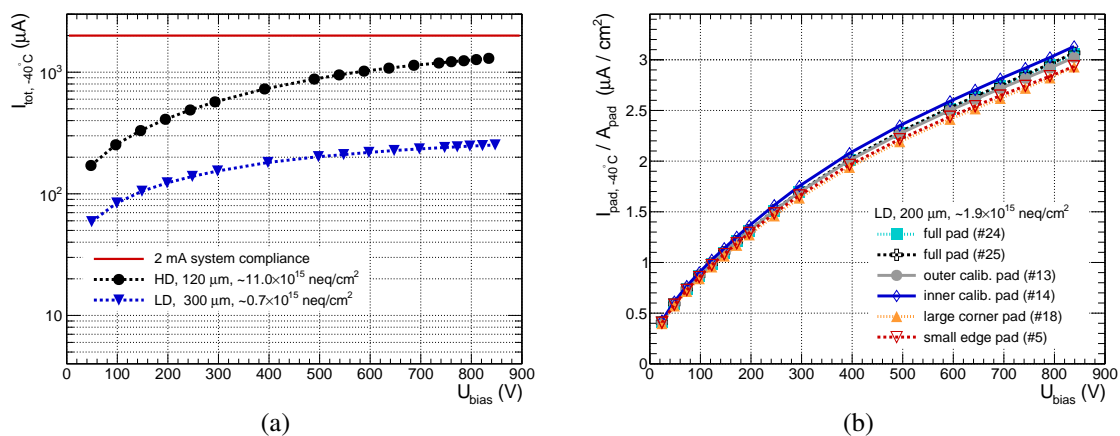[1]Corresponding to about three years at 0 °C.

Figure 6. (a) Total leakage currents after irradiation (without additional thermal annealing) for two representative example sensors. Currents were measured at $-40\,^{\circ}\text{C}$ ($I_{\text{tot, }-40\,^{\circ}\text{C}}$) and at different effective bias voltages (U_{bias}). (b) Per-pad leakage currents normalised to the area of full hexagonal pads as a function of the bias voltage for different pads with different geometries on one example sensor.

studied sensors were cooled again to $-40\,^{\circ}\text{C}$. IV and CV characterisations were conducted before and after additional annealing.

5 Results

The results of the electrical characterisation of the neutron-irradiated CE silicon pad sensor prototypes are presented in this section. Section 5.1 focuses on the discussion of leakage currents (*IV*) whereas section 5.2 addresses the capacitance (*CV*) and depletion voltage assessments. Section 5.3 offers a discussion on the drawn conclusion.

5.1 Leakage current

The total leakage current, interpreted as the dark current of a full silicon sensor, is defined as the current flowing through the high-voltage resistor R_{HV} (cf. figure 2 in [11]). As it is shown for two prototype sensors in figure 6(a), the total leakage current did not break down and stayed well below the ARRAY system's compliance of 2 mA for the irradiated sensors discussed in this paper. Irreversible discharges are undesired but occurred for a handful of sensors where the total leakage current suddenly increased and exceeded the 2 mA limitation. One half of those instances could be traced back to mechanical damages, e.g. induced during the transport or sensor handling, and the other half hinted at the presence of a minor flaw in the CE silicon sensor design. The latter ultimately lead to a design modification with which the risk of discharges in the future should be minimised[2]. Results of the affected sensors are not discussed further in this paper.

Figure 6(b) shows the per-pad leakage current as a function of the effective bias voltage for adjacent pads of various sizes on a low density sensor irradiated up to $\sim 1.9 \times 10^{15}$ $n_{\text{eq}}/\text{cm}^2$. The data demonstrate that, in good approximation, the leakage current of a pad scales with its

---

[2]More than 50 prototype sensors with the improved design have been characterized with voltages up to 850 V in the meantime. None have shown discharges thus far.
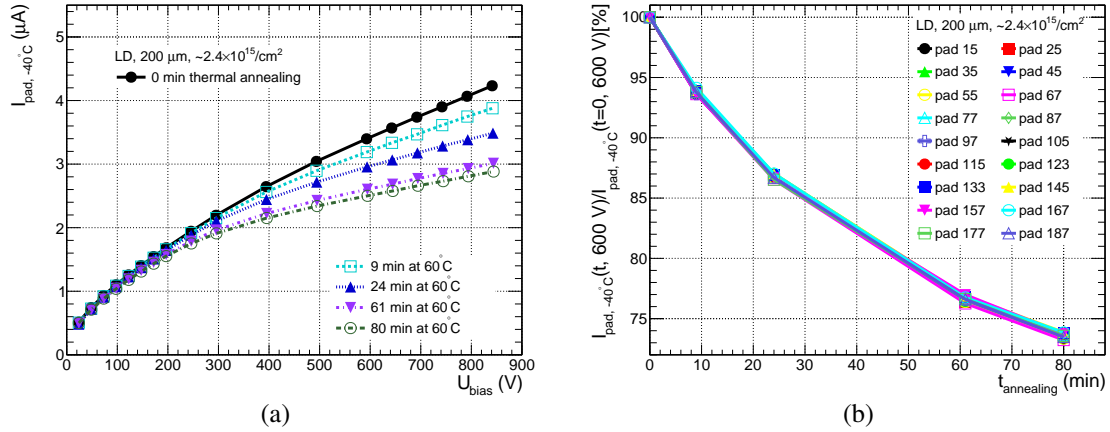
Figure 7. (a) IV-curves of a representative full hexagonal pad for different annealing durations for a 200 µm low-density prototype sensor irradiated to approximately 2.4×10^{15} n_{eq}/cm^2. (b) Decrease of the per-pad leakage current ($U_{bias} = 600$ V) as a function of the annealing time ($t_{annealing}$) at 60 °C.

volume. The relative increase from 600 V to 800 V remains well below 150 % meeting the vendor specifications.

The IV curves after different annealing times are shown for a representative pad in figure 7(a). For bias voltages beyond full depletion, per-pad leakage currents at 600 V are reduced systematically by 25 % after 80 min at 60 °C, cf. figure 7(b). Given the simultaneous reduction in the depletion voltage, cf. figure 10(b), leakage currents around full depletion are even further reduced.

The expected relationship between the per-pad leakage current density and the fluence was observed. The proportionality for current densities at a bias voltage of 600 V, which is well above full depletion for all investigated sensors (except for the 300 µm sensors irradiated to $13.5 \times 10^{14} n_{eq}/cm^2$), and extrapolated to −30 °C is displayed in figure 8. As expected [18], the current-related damage rate (α) is found to be independent on the tested material properties investigated in this work. The numerical result for α scaled to room temperature is $\alpha_{600V}(20 °C) = (3.2 \pm 0.2 \pm 0.6) \times 10^{-17}$ A/cm. The central value is about 20 % less than what is reported in ref. [13]. A possible explanation could be a systematic overestimation of the fluence at the RINSC irradiation facility. Follow-up studies in this regard are anticipated in the mid-term future.

After correction for the chuck temperature non-uniformity, per-pad leakage current densities across a sensor at a fixed voltage still vary by ∼ 10 %. The associated current profiles are present both before (cf. figure 9(a) to 9(c)) and after additional annealing (cf. figure 9(d) to 9(f)). Furthermore, they are consistent between sensors that had been irradiated simultaneously in the same puck. Among others, a plausible explanation for this observation could be the presence of a fluence profile within the beam port at RINSC that can be approximated as a Gaussian with a width of $\sigma \sim 10$ cm.

5.2 Capacitance and depletion voltage

The measured per-channel impedance is open-corrected by subtracting the impedance of the AR-RAY system. Subsequently, the sensor pad capacitance is computed assuming an underlying serial connection to the measurement circuitry. Due to the finite mobility of the sensor defects, the
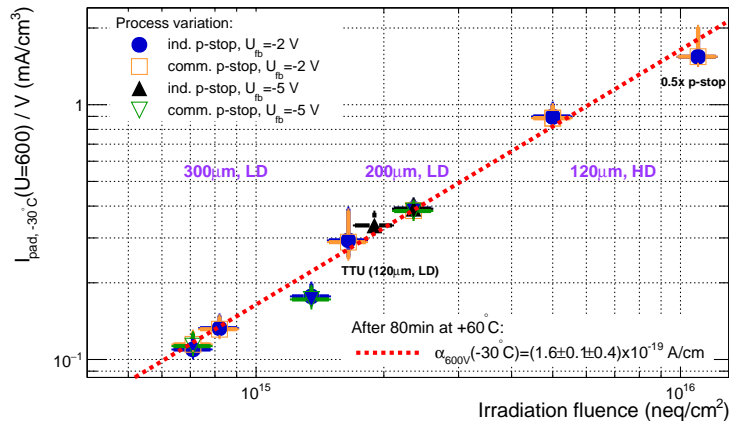
Figure 8. Volume-normalised per-pad leakage currents interpolated to an effective bias voltage of 600 V as a function of the fluence that they were exposed to. The quoted currents were measured after additional annealing at 60 °C, and are scaled to the CE's planned operation temperature of −30 °C. "0.5x p-stop" denotes HD sensors with half the p-stop concentration. "TTU" denotes the measurements of 120 μm HD sensors conducted with a analogous setup to the one described in section 4.1, at Texas Tech University. Those exhibit overall consistency with the measurements conducted at CERN.
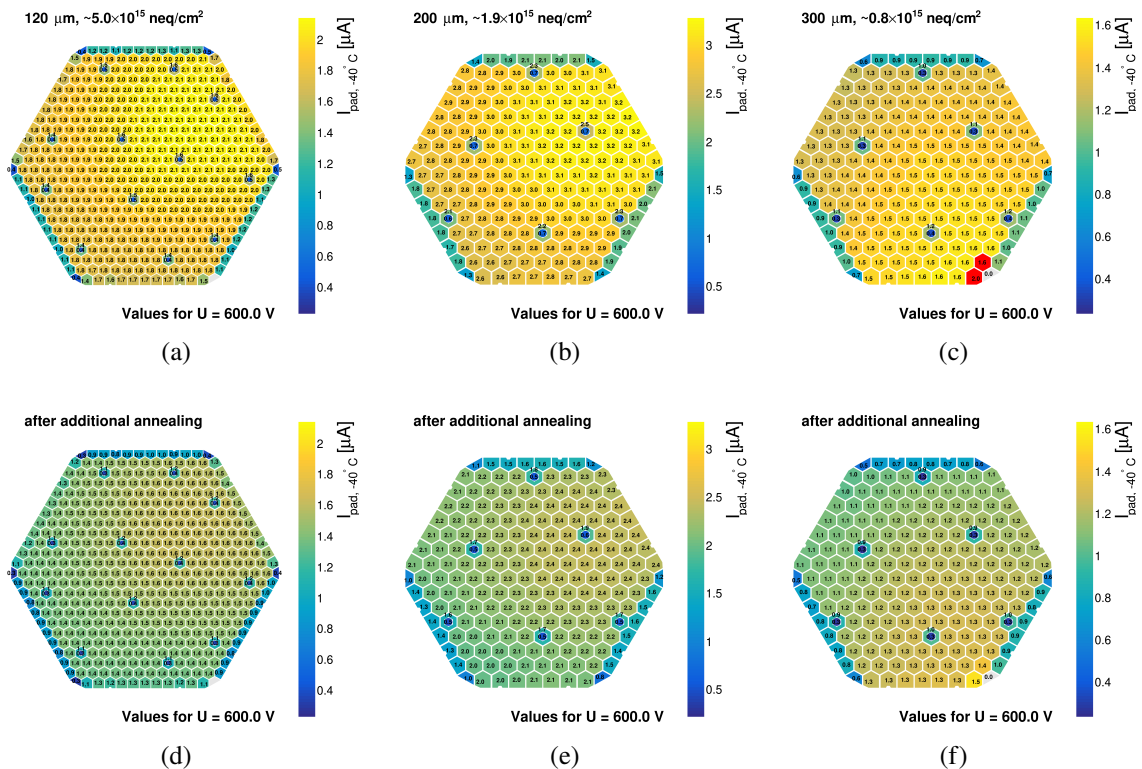

Figure 9. Per-pad leakage currents interpolated to an effective bias voltage of 600 V for three representative sensors from different irradiation rounds before (a-c) and after additional annealing (d-f). Red- or white-colored edge pads correspond to well-understood measurement effects, e.g. insufficient contact between the pogo pins and the pads.
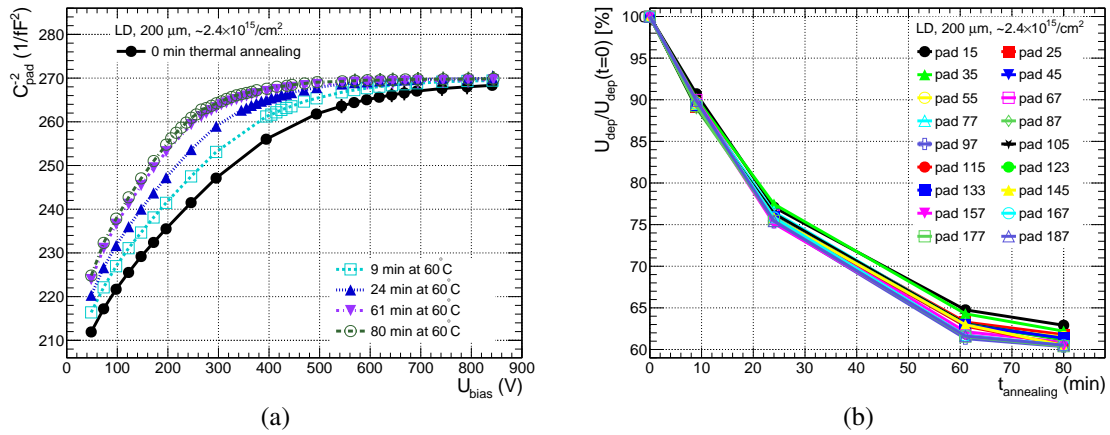
Figure 10. (a) Reciprocal-squared capacitance (C_{pad}^{-2}) as a function the bias voltage of a representative full hexagonal pad for different annealing durations for a 200 µm low-density prototype sensor irradiated to approximately $2.4{\times}10^{15}$ n_{eq}/cm^2. (b) Relative decrease of the depletion voltage estimate (U_{dep}) as a function of the additional annealing time ($t_{annealing}$) at 60 °C for a subset of full pads.

frequency at which the impedance is measured may, in principle, have sizeable impact on the derived capacitance and on the depletion voltages, cf. ref. [19]. The impedance measurement was conducted at $f_{LCR} = 2\,kHz$. Experimental follow-up indicated an impact of 2 % on the asymptotic capacitance and a 10 % reduction of the depletion voltage when decreasing f_{LCR} to 500 Hz, which have no implication on the following discussion.

The depletion voltage for each pad is assessed from the saturation of its squared reciprocal capacitance (C^{-2}) of a pad with respect to the bias voltage (V). It is defined as the intersection of a straight-line fitted to the rising part of the C^{-2} vs. V curve with a line fitted to its plateau. Prior to additional annealing, such a plateau could not always be reached within the tested bias voltage range, see for example the black line in figure 10(a). After additional annealing to 80 min at 60 °C, the estimated depletion voltage has been reduced by about a third with respect to the case without annealing, cf. figure 10(b).

The per-pad capacitance after irradiation is found to scale well with the area of the pad, cf. figure 11(a).

Deviations from this scaling amount to less than 5 %, suggesting a slight dependence of the inter-pad capacitances on the pad geometries.

Figure 11(b) illustrates that the estimated depletion voltages depend primarily on the associated thickness of the depleted zone. The estimated per-pad depletion voltage across the sensor is shown in figure 12(a). Those estimates exhibit positive correlation with the leakage currents, taken as proxy for the fluence, cf. figure 12(b). In fact, the obtained correlation coefficient from this analysis is positive for all tested sensors where full depletion could be reached. This can be interpreted as further evidence for the presence of a fluence profile inside the beam port during irradiation.

5.3 Discussion

The neutron irradiation induced leakage currents are consistent both qualitatively and quantitatively with previous R&D on irradiated silicon sensors. They are also found to be independent of
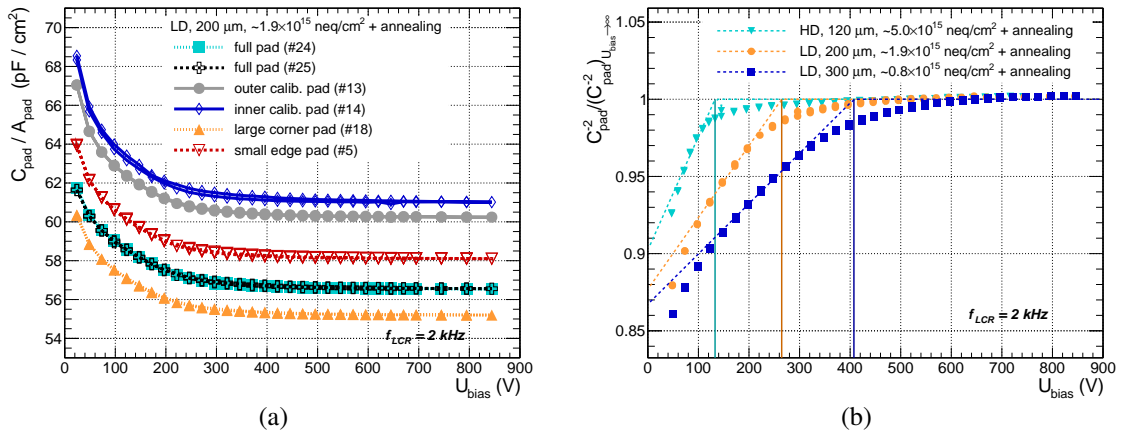
Figure 11. (a) Area-normalised capacitances as a function of the bias voltage for different pads with different geometries on a example LD sensor. (b) Normalised squared-inverse capacitances as a function of the bias voltage to estimate the sensor depletion voltage of a central pad from different irradiation rounds. Full depletion was achieved at bias voltages around 40 V for 120 μm sensors, 120 V for 200 μm sensors, and 280 V for the 300 μm sensors before irradiation.
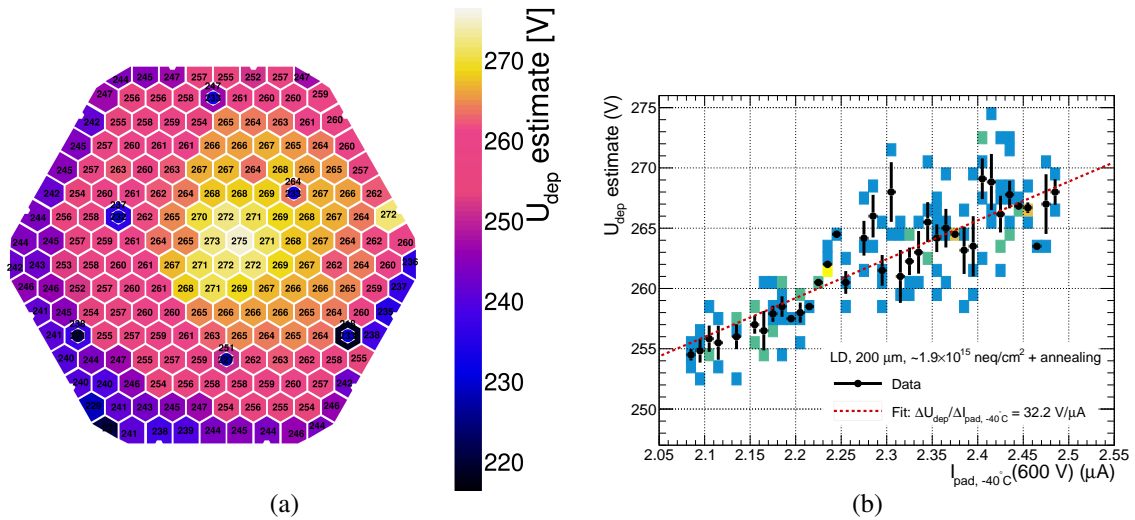

Figure 12. (a) Per-pad depletion voltage estimates for a 200 μm LD example sensor irradiated to 1.9×10^{15} n_{eq}/cm^2, and (b) their correlation to the per-pad leakage current, used as proxy for the delivered fluence.

the silicon fabrication process (flatband voltage, p-stop layout). Furthermore, unchanged end-capacitances and reduced depletion voltages after beneficial annealing are qualitatively consistent with previous findings.

The findings presented in this paper with the first prototypes of CE silicon sensors, i.e. hexagonal sensors and fabricated with a new 8" process, irradiated to fluences corresponding to the end of lifetime of HL-LHC are in full support of the radiation-hardness of their general design. By implication, RINSC could be qualified as a valid facility for neutron irradiation of 8" silicon sensors for the first time. However, more accurate studies on the electrical sensor properties after neutron-

irradiation would need to incorporate the systematic uncertainty on the effective annealing during irradiation, that is due to the temperature evolution and its potential lateral profile inside the reactor's beam port. Similarly, an accurate assessment of the actual fluence at each pad would have to address the neutron flux profile, for whose existence this work provides first evidence.

6 Conclusion

An essential component of the silicon sensors' prototyping for the CMS highly granular endcap calorimeter upgrade (CE) is the experimental verification of the radiation hardness in terms of their electrical properties, i.e. leakage currents, capacitances and depletion voltages. RINSC is one of the few locations world-wide that offers the infrastructure for the irradiation of large structures compatible with CE's 8"-wide silicon pad sensors. Given that parts of the necessary infrastructure have not been used in this experimental capacity, the irradiation was non-trivial and specific preparations had to be made. After irradiation, the probe- and switch card-based ARRAY system [11] was used for the first time for the electrical characterisation of neutron-irradiated silicon sensors at CERN and at Texas Tech University. In order to protect the test system from currents that would exceed its specifications, the neutron-irradiated sensors were cooled down to $-40\,^\circ$C during the tests.

The preparation and execution of the neutron-irradiation at RINSC and the electrical characterisation of the irradiated sensors at cold temperatures using the ARRAY system was explained in this paper. Evidence for specific properties of the RINSC irradiation facility such as a non-uniform flux profile across the 8" wafer and for non-negligible sensor annealing due to insufficient cooling during irradiation was reported.

For the planned CMS CE upgrade, the findings in this work are encouraging as they confirm the overall expected radiation hardness of the prototype silicon sensors. In particular, their leakage current densities are found to scale proportionally with the fluence, independent of the properties of the tested production process variations. It is reconfirmed that annealing the sensors up to 80 min at $60\,^\circ$C has beneficial impact on the electrical properties by lowering the dark current and the depletion voltages by $O\,(10\,\%)$. Despite the tested sensors being prototypes, the insights from their characterisation can be considered representative for the final version. Therefore, the results reported in this work may serve as reference for the expected electrical performance and degradation of CE's silicon sensors towards the end of their lifetime at HL-LHC.

A   Irradiation rounds and fluences

See table 1.

Table 1. Irradiation duration and estimated integrated fluences for the neutron-irradiation at RINSC of CE prototype silicon sensors discussed in this work. A comparison to leakage currents of silicon test structures irradiated at the JSI TRIGA reactor [20] indicate an uncertainty on the fluence estimates of about 20 %.

Date	No. sensors	Thickness	Duration	Fluence (10^{14} n_{eq}/cm^2)	Reference
26 Aug 20	4	300 μm	13 min	7.1	Si diodes
20 Oct 20	4	120 μm	180 min	110.0	Fe foils
28 Jan 21	4	200 μm	38 min	23.5	Si diodes
11 Feb 21	4	120 μm	38 min	16.5	Si diodes
01 March 21	4	300 μm	23 min	13.5	Si diodes
11 March 21	4	120 μm	76 min	50.0	Fe foils
15 April 21	4	300 μm	15 min	8.2	Si diodes
06 May 21	2	200 μm	38 min	19.0	Si diodes

B   Temperature uniformity of the systems att C200-40 cold chuck

The leakage current in silicon devices dependends on the temperature. For the investigated sensors in this work, the current is mainly generated in the bulk for which the temperature (T) and current (I) are related by eq. (B.1) [21], where $E_{eff} = 1.21$ eV is the effective gap energy and k_b denotes the Boltzmann constant.

$$\frac{I}{T^2} \cdot \exp \frac{E_{eff}}{2 \cdot k_b \cdot T} \equiv \text{const.} \tag{B.1}$$

The validity of this temperature scaling law applied for the CE silicon pad sensors in the relevant temperature range has been verified and is illustrated in figure 13. Notably, a change by 1 °C impacts the current by more than 10 %. Variations of the temperature across the actively cooled-down chuck, and with it across the sensor, may mimic neutron fluence profiles as in figure 9. Thus, they should be identified and corrected for.

In this work, the temperature non-uniformity of the cold chuck at CERN (C200-40 model produced by Systems att) could be estimated from leakage current data of neutron-irradiated sensors. By comparing per-pad currents ($I_{i(j,k)}$) at a fixed bias voltage between the symmetry locations i, j, k, described below, temperature differences $\delta I_{i(j),k}$ can be calculated according to eq. (B.2). For this purpose, one of the neutron-irradiated low-density sensors was characterised three times at
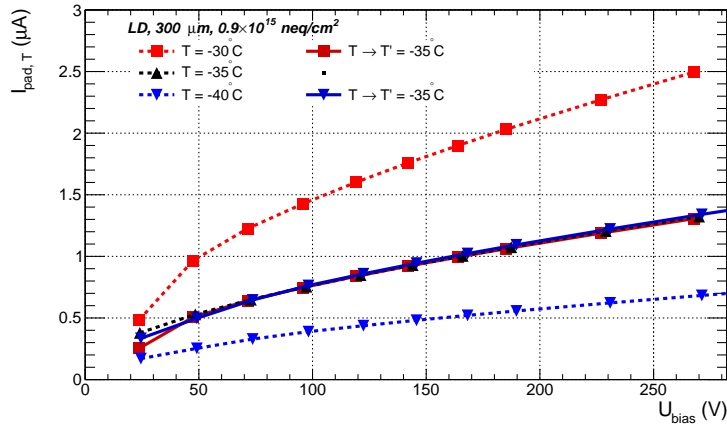
Figure 13. Leakage currents as a function of the bias voltage for an example sensor measured at $-40\,°C$, $-35\,°C$, $-30\,°C$, and scaled to $-35\,°C$ using eq. (B.1).

(a)   (b)   (c)
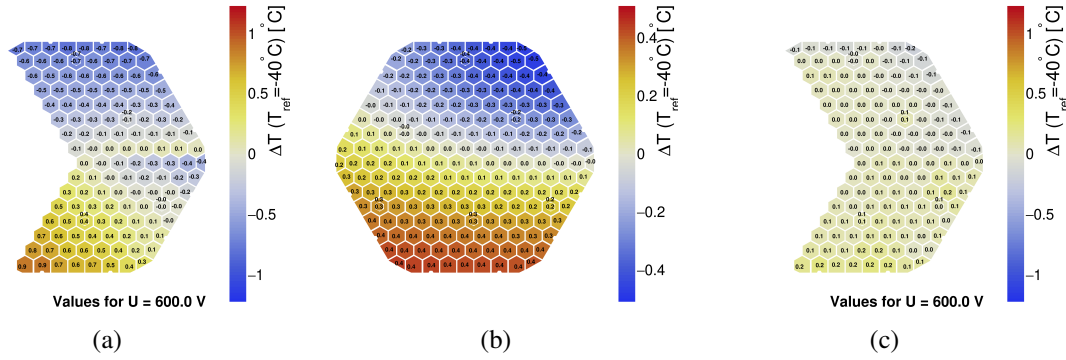
Figure 14. (a) Temperature differences derived from per-pad leakage currents between symmetric locations of a representative neutron-irradiated CE silicon sensors on the cold chuck at CERN. (b) Determined profile of temperature differences, modelled as a two-dimensional gaussian, across the sensor surface. (c) Closure check: derived temperature differences after accordingly correcting the measured per-pad leakage currents.

$0°$, $120°$, and $240°$ rotation. The precision in repeating the sensor placement on the chuck can be neglected with respect to the size of the pads.

$$\frac{\delta I_{i(j),k}}{I_k} = \frac{\delta T_{i(j),k}}{T_k} \cdot \left(2 + \frac{E_{\text{eff}}}{2 \cdot k_b \cdot T_k}\right), \quad T_k := T_{\text{ref}} \tag{B.2}$$

Figure 14(a) shows the hereby computed chuck temperature differences. The determined variation is consistent with the $\pm 0.5\,°C$ non-uniformity as specified by the chuck producer. Assuming a reference temperature of $T_{\text{ref}} \equiv -40\,°C$, a two-dimensional gaussian parameterisation bound to $[-0.5\,°C, 0.5\,°C]$ is fitted to reproduce the temperature differences $\delta I_{i(j),k}$. The result of the fit is shown in figure 14(b). The hereby constructed map of chuck temperature differences is input to correct the measured per-pad leakage currents using eq. (B.1). As a closure check, the re-application of eq. (B.2) on the temperature-corrected dataset demonstrates the applicability of this particular chuck temperature model as shown in figure 14(c).

References

[1] L. Evans and P. Bryant, *LHC Machine*, 2008 *JINST* **3** S08001.

[2] I. Zurbano Fernandez et al., *High-Luminosity Large Hadron Collider (HL-LHC): Technical design report*, CERN-2020-010 (2020) [DOI:10.23731/CYRM-2020-0010].

[3] CMS collaboration, *The CMS Experiment at the CERN LHC*, 2008 *JINST* **3** S08004 [INSPIRE].

[4] CMS collaboration, *The Phase-2 Upgrade of the CMS Endcap Calorimeter*, CERN-LHCC-2017-023, CERN, Geneva (2017) [DOI:10.17181/CERN.IV8M.1JY2].

[5] N. Akchurin et al., *First beam tests of prototype silicon modules for the CMS High Granularity Endcap Calorimeter*, 2018 *JINST* **13** P10023.

[6] CMS HGCAL collaboration, *The DAQ system of the 12,000 channel CMS high granularity calorimeter prototype*, 2021 *JINST* **16** T04001 [arXiv:2012.03876] [INSPIRE].

[7] CMS HGCAL collaboration, *Construction and commissioning of CMS CE prototype silicon modules*, 2021 *JINST* **16** T04002 [arXiv:2012.06336] [INSPIRE].

[8] B. Acar et al., *Response of a CMS HGCAL silicon-pad electromagnetic calorimeter prototype to 20–300 GeV positrons*, 2020 *JINST* **17** P05022.

[9] E. Currás et al., *Radiation hardness study of Silicon Detectors for the CMS High Granularity Calorimeter (HGCAL)*, 2017 *JINST* **12** C02056.

[10] N. Akchurin et al., *Charge collection and electrical characterization of neutron irradiated silicon pad detectors for the CMS High Granularity Calorimeter*, 2020 *JINST* **15** P09031 [arXiv:2005.08051].

[11] E. Brondolin et al., *ARRAY: an open source, modular and probe-card based system with integrated switching matrix for characterisation of large area silicon pad sensors*, *Nucl. Instrum. Meth. A* **940** (2019) 168 [arXiv:1903.10262].

[12] CMS collaboration, *P-type silicon strip sensors for the new CMS tracker at HL-LHC*, 2017 *JINST* **12** P06018 [INSPIRE].

[13] M. Moll, *Displacement damage in silicon detectors for high energy physics*, *IEEE Trans. Nucl. Sci.* **65** (2018) 1561.

[14] G. Lindstrom, *Radiation damage in silicon detectors*, *Nucl. Instrum. Meth. A* **512** (2003) 30 [INSPIRE].

[15] A. Bean et al., *Studies on the radiation damage to silicon detectors for use in the D0 Run2b experiment*, D0 Note 3958, (2002).

[16] A. Maier et al., *HexDAQ*, version: v1.5.1, (2022).

[17] M. Moll, *Radiation damage in silicon particle detectors: Microscopic defects and macroscopic properties*, Ph.D. thesis, Hamburg University, Germany (1999) [INSPIRE].

[18] CERN-ROSE/RD48 collaboration, *Leakage current of hadron irradiated silicon detectors — material dependence*, *Nucl. Instrum. Meth. A* **426** (1999) 87 [INSPIRE].

[19] Z. Li and H.W. Kraner, *Studies of frequency dependent C-V characteristics of neutron irradiated $p^{\pm}n$ silicon detectors*, *IEEE Trans. Nucl. Sci.* **38** (1991) 244.

[20] V. Radulovic et al., *Large object irradiation facility in the tangential channel of the JSI TRIGA reactor*, AIDA-2020-CONF-2017-003, (2017).

[21] A. Chilingarov, *Temperature dependence of the current generated in Si bulk*, 2013 *JINST* **8** P10003.

The CMS HGCAL collaboration

B. Acar [2], G. Adamov[16], C. Adloff[32], S. Afanasiev [45], N. Akchurin [41], B. Akgün [2],
M. Alhusseini [24], J. Alison [6], J. P. Figueiredo de sa Sousa de Almeida[5], P. G. Dias de Almeida[5], A.
Alpana[20], M. Alyari [10], I. Andreev[45], U. Aras[2], P. Aspell[5], I. O. Atakisi[2], O. Bach[9], A. Baden[28],
G. Bakas [33], A. Bakshi[10], S. Banerjee [43], P. DeBarbaro[36], P. Bargassa [26], D. Barney [5],
F. Beaudette [25], F. Beaujean[25], E. Becheva[25], A. Becker[5], P. Behera [21], A. Belloni [28], T. Bergauer [18],
M. El Berni[35], M. Besancon [37], S. Bhattacharya [30], S. Bhattacharya [38], D. Bhowmik[38], B. Bilki [24],
F. Blekman [9], P. Bloch [22], A. Bodek [36], M. Bonanomi [17], A. Bonnemaison[25], S. Bonomally[22],
J. Borg [22], F. Bouyjou[37], N. Bower [13], D. Braga [10], L. Brennan[42], E. Brondolin [5], P. Bryant [6],
A. Butler-Nalin[42], O. Bychkova[45], S. Callier[35], D. Calvet[37], K. Canderan[5], K. Cankocak [23], X. Cao[19],
A. Cappati [25], B. Caraway [1], S. Caregari[32], C. Carty[41], A. Cauchois[25], L. Ceard[34], D. Sunar Cerci [23],
S. Cerci [23], G. Cerminara [5], M. Chadeeva [45], N. Charitonidis[5], R. Chatterjee[29], J. A. Chen[34],
Y. M. Chen [28], H. J. Cheng [34], K. Y. Cheng[32], H. Cheung [10], D. Chokheli [16], M. Cipriani [5],
D. Čoko [11], F. Couderc [37], E. Cuba[5], M. Danilov [45], D. Dannheim [5], W. Daoud[25], I. Das [39],
P. Dauncey [22], G. Davies [22], O. Davignon [25], E. Day[6], P. Debbins [24], M. M. Defranchis [5],
E. Delagnes[37], Z. Demiragli [3], U. Demirbas[2], G. Derylo[10], D. Diaz [13], L. Diehl [5], P. Dinaucourt[35],
G. G. Dincer[23], J. Dittmann [1], M. Dragicevic [18], S. Dugad[39], F. Dulucq[35], I. Dumanoglu[8], M. Dünser[5],
S. Dutta [38], V. Dutta [42], T. K. Edberg[28], F. Elias[27], S. C. Eno [28], Yu. Ershov[45], S. Extier [35],
F. Fahim [10], C. Fallon[36], G. Fedi [22], L. Ferragina[5], L. Forthomme [5], E. Frahm[29], G. Franzoni [5],
J. Freeman [10], T. French[5], P. Gandhi[10], S. Ganjour [37], X. Gao [14], M. T. Ramos Garcia[5],
A. Garcia-Bellido [36], F. Gastaldi[25], D. Gastler [3], Z. Gecse [10], A. Germer[6], H. Gerwig[5], O. Gevin[37],
S. Ghosh [25], A. Gilbert [30], W. Gilbert[29], K. Gill [5], C. Gingu [10], S. Gninenko[45], A. Golunov[45],
I. Golutvin [45], B. Gonultas[2], N. Gorbounov[45], L. Gouskos [5], A. B. Gray[5], C. Grieco [42],
S. Grönroos [5], Y. Gu[19], F. Guilloux [37], E. Gurpinar Guler[8], Y. Guler[8], E. Gülmez [2], J. Guo[19],
H. Gutti[10], A. Hakimi [25], M. Hammer [10], H. M. Hassanshahi [22], K. Hatakeyama [1], E. Hazen[3],
A. Heering[31], V. Hegde [41], U. Heintz[4], N. Hinton[4], J. Hirschauer [10], J. Hoff[10], W.-S. Hou[34], X. Hou[19],
H. Hua[19], A. Hussain [41], J. Incandela[42], A. Irshad[5], C. Isik[8], S. Jain [29], J. Jaroslavceva[5], H. R. Jheng[32],
U. Joshi [10], K. Kaadze [15], V. Kachanov[45], L. Kalipoliti [25], A. Kaminskiy[45], A. R. Kanuganti [1],
Y.-W. Kao[34], A. Kapoor [19], O. Kara[8], A. Karneyeu [45], O. Kałuzińska [5], M. Kaya [2], O. Kaya [2],
Y. Kazhykharim[41], F. A. Khan [5], A. Khukhunaishvili [36], J. Kieseler [5], M. Kilpatrick [42], S. Kim [13],
K. Koetz[13], T. Kolberg [13], M. Komm [9], O. K. Köseyan[24], V. Kraus[18], M. Krawczyk [5],
K. Kristiansen[42], A. Kristić [11], M. Krohn [29], B. Kronheim[28], K. Krüger[9], S. Kulis [5], M. Kumar [39],
S. Kunori[41], C. M. Kuo[32], V. Kuryatkov[41], S. Kyre[42], Y. Lai [28], K. Lamichhane [41], G. Landsberg [4],
C. Lange [5], J. Langford [22], M. Y. Lee[32], S.-W. Lee[41], A. G. Stahl Leiton [5], A. Levin[45], A. Li [42],
J. H. Li[9], Y. Y. Li[34], Z. Liang[40], H. Liao [19], Z. Lin [44], D. Lincoln [10], L. Linssen [5], R. Lipton[10],
G. Liu [25], Y. Liu [19], A. Lobanov[17], V. Lohezic[37], D. Lomidze [16], R.-S. Lu[34], M. Lupi [5],
I. Lysova[45], A.-M. Magnan [22], F. Magniette[25], A. Mahjoub[25], B. Meier [5], A. Malakhov [45], S. Mallios[5],
I. Mandjavize[37], M. Mannelli [5], J. Mans [29], A. Marchioro[5], A. Martelli [22], G. Martinez[13],
P. Masterson [42], M. Matthewman[5], S. N. Mayekar[39], A. David [5], S. Coco Mendez[5], B. Meng[19],
A .Menkel[41], A. Mestvirishvili[24], G. Milella [9], I. Mirza[39], S. Moccia[5], G. B. Mohanty [39],
F. Monti [19], F. W. Moortgat [5], I. Morrissey[29], J. Motta [25], S. Murthy[6], J. Musić [11],
Y. Musienko [31], S. Nabili [28], M. Nguyen[25], A. Nikitenko [45], D. Noonan [12], D. Noonan[10], M. Noy[5],

K. Nurdan[2], M. Wulansatiti Nursanto[13], C. Ochando [25], N. Odell[30], H. Okawa [14], Y. Onel[24], W. Ortez[42], J. Ozegović [11], S. Ozkorucuklu [23], E. Paganis [34], C. A. Palmer [28], S. Pandey [20], F. Pantaleo [5], C. Papageorgakis [28], I. Papakrivopoulos[33], M. Paranjpe[28], J. Parshook[6], N. Pastika [10], M. Paulini [6], T. Peltola [41], N. Peng[19], A. Buchot Perraguin[25], P. Petiot[5], T. Pierre-Emile[25], M. Vicente Barreto Pinto [5], E. Popova [45], H. Prosper [13], M. Prvan [11], I. Puljak [11], S. R. Qasim[5], H. Qu [5], T. Quast [5], R. Quinn [29], M. Quinnan [42], K. K. Rao[39], K. Rapacz[5], L. Raux[35], W. Redjeb [5], M. Reinecke[9], M. Revering [29], A. Roberts [6], A. M. Sanchez Rodriguez[5], J. Rohlf [3], T. Romanteau[25], M. Rosado[5], A. Rose [22], M. Rovere [5], A. Roy [32], P. Rubinov [10], R. Rusack [29], V. Rusinov[45], V. Ryjov[5], O. M. Sahin[37], R. Salerno [25], R. Saradhy [29], K. Sarbandi [5], T. Sarkar [32], M. A. Sarkisla[2], J. B. Sauvan[25], I. Schmidt[24], M. Schmitt [30], E. Scott [22], C. Seez [22], F. Sefkow[9], D. Selivanova [9], S. Sharma [20], M. Shelake[39], A. Shenai[10], R. Shukla [22], E. Sicking [5], M. De Silva[9], P. Silva [5], P. Simkina [37], A. E. Simsek[8], Y. Sirois [25], V. Smirnov [45], T. J. Sobering[15], E. Spencer[4], N. Srimanobhas [7], A. Steen [34], J. Strait[10], N. Strobbe [29], X. F. Su[34], C. Mantilla Suarez[10], E. Sukhov[45], L. Sulak[3], L. Sun[19], P. Suryadevara[39], C. Syal[10], C. de La Taille[35], B. Tali[8], C. L. Tan[36], J. Tao [19], A. Tarabini[25], T. Tatli[2], R. Thaus[36], R. D. Taylor[15], S. Tekten [2], D. Thienpont[35], C. Tiley[4], E. Tiras [24], M. Titov[37], D. Tlisov [45], U. G. Tok[8], A. Kayis Topaksu[8], J. Troska [5], L.-S. Tsai[34], Z. Tsamalaidze [16], G. Tsipolitis[33], A. Tsirou[5], S. Undleeb [41], D. Urbanski[29], E. Uslan[8], V. Ustinov[45], A. Uzunian[45], J. Varela [26], M. Velasco[30], E. Vernazza [25], O. Viazlo [13], P. Vichoudis[5], T. Virdee [22], E. Voirin[10], M. Vojinoviç [5], M. Vojinovic [22], A. Wade[13], C. Wang[19], C.C. Wang[19], D. Wang [40], F. Wang[19], X. Wang[10], X. Wang[40], Z. Wang[19], M. Wayne [31], S. N. Webb [22], A. Whitbeck [41], R. Wickwire [10], J. S. Wilson [1], H. Y. Wu[34], L. Wu [19], M. Xiao [44], J. Yang[42], C. H Yeh[32], R. Yohay [13], D. Yu [4], S. S. Yu [32], C. Yuan [19], Y. Miao[30], F. Yumiceva [12], I. Yusuff[27], A. Zabi [25], A. Zacharopoulou[33], N. Zamiatin[45], A. Zarubin [45], P. Zehetner [5], H. Zhang [19], J. Zhang[13], Y. Zhang [14], Z. Zhang[19], X. Zhao[19]

1 *Baylor University, Waco 76706, TX, USA*

2 *Boğaziçi University, Bebek 34342, Istanbul, Turkey*

3 *Boston University, Boston, Massachusetts, USA*

4 *Brown University, 182 Hope Street, Providence 02912, RI, USA*

5 *CERN,Espl. des Particules 1, 1211 Geneve 23, Switzerland*

6 *Carnegie Mellon University, 5000 Forbes Ave, Pittsburgh 15213, PA, USA*

7 *Chulalongkorn University ,Department of Physics, Faculty of Science, 10330, Phatumwan, Bangkok*

8 *Çukurova University, 01330, Adana, Turkey*

9 *Deutsches Elektronen-Synchrotron DESY, Notkestr. 85 22607, Hamburg, Germany*

10 *Fermilab, Wilson Road, Batavia 60510, IL, USA*

11 *University of Split FESB, R. Boskovica 32, HR-21000, Split, Croatia*

12 *Florida Institute of Technology, 150 W University Blvd, Melbourne 32901, FL, USA*

13 *Florida State University, 600 W. College Ave., Tallahassee 32306, FL, USA*

14 *Fudan University, 220 Handan Road, Yangpu, Shanghai 200433, China*

15 *Kansas State University, 116 Cardwell Hall, Physics Department, Manhattan, KS 66506-2601, USA*

16 *Georgian Technical University, 77 Kostava Str 0175, Tbilisi, Georgia*

17 *The University of Hamburg, Institut für Experimentalphysik, Luruper Chaussee 149, 22761 Hamburg, Germany*

18 *HEPHY Vienna,Nikolsdorfer Gasse 18, 1050 Wien, Vienna, Austria*

19 *IHEP Beijing, 19 Yuquan Road, Shijing Shan, China*

20 *Indian Institute of Science Education and Research, Dr. Homi Bhabha Road 411008, Pune, India*

21 *Indian Institute of Technology, 60036 Chennai, India*

22 *Imperial College,Prince Consort Road SW7 2AZ, London, United Kingdom*

23 *Istanbul Technical University, 34134 Vezneciler-Fatih, Istanbul, Turkey*

24 *The University of Iowa, 203 Van Allen Hall, Iowa City, 52242, Iowa, USA*

25 *Laboratoire Leprince-Ringuet CNRS/IN2P3, Route de Saclay, 91128 Ecole Polytechnique, France*

26 *LIP, Avenida Prof. Gama Pinto, n° 2, 1649-003, Lisbon, Portugal*

27 *National Centre for Particle Physics,University of Malaya,Kuala Lumpur 50603,Malaysia*

28 *The University of Maryland, College Park 20742, MD, USA*

29 *The University of Minnesota, 116 Church Street SE, Minneapolis 55405, MN, USA*

30 *Northwestern University,2145 Sheridan Rd, Evanston 60208, IL, USA*

31 *University of Notre Dame, Notre Dame 46556, IN, USA*

32 *National Central University Taipei (NCU),No.300, Jhongda Rd 32001, Jhongli City, Taiwan*

33 *National Technical University of Athens, 9, Heroon Polytechneiou Street 15780, Athens, Greece*

34 *National Taiwan University, 10617, Taipei, Taiwan*

35 *Laboratoire OMEGA CNRS/IN2P3, Route de Saclay 91128, Ecole Polytechnique, France*

36 *University of Rochester, Campus Box 270171, Rochester 14627, NY, USA*

37 *CEA Paris-Saclay, IRFU, Batiment 141,91191, Gif-Sur-Yvette Paris, France*

38 *SINP, Sector 1 Block AF, Bidhan Nagar, 700 064, Kolkata, India*

39 *Tata Inst. of Fundamental Research,Homi Bhabha Road, Mumbai 400005, India*

40 *Tsinghua University, Department of Physics, Beijing, 100084, China*

41 *Texas Tech University, Lubbock 79409, TX, USA*

42 *UC Santa Barbara, Santa Barbara 93106, CA, USA*

43 *The University of Wisconsin, Madison, WI, USA*

44 *Zhejiang University,Department of Physics, 38 Zheda Road, Hangzhou,ZHEIJIANG 310027, CHINA*

45 *Affiliated with an institute or an international laboratory covered by a cooperation agreement with CERN*